Monthly Notices of the ROYAL ASTRONOMICAL SOCIETY

Mon. Not. R. Astron. Soc. **427,** 651–663 (2012) doi:10.1111/j.1365-2966.2012.21867.x

The nature of the unresolved extragalactic cosmic soft X-ray background

N. Cappelluti,[1,2★] P. Ranalli,[1,3,4] M. Roncarelli,[4] P. Arevalo,[5] G. Zamorani,[1] A. Comastri,[1] R. Gilli,[1] E. Rovilos,[1] C. Vignali,[1,4] V. Allevato,[6] A. Finoguenov,[2,7] T. Miyaji,[8] F. Nicastro,[9] I. Georgantopoulos[1,3] and A. Kashlinsky[10,11]

[1]*INAF–Osservatorio Astronomico di Bologna, Via Ranzani 1, 40127 Bologna, Italy*
[2]*University of Maryland, Baltimore County, 1000 Hilltop Circle, Baltimore, MD 21250, USA*
[3]*Institute of Astronomy and Astrophysics, National Observatory of Athens, Palaia Penteli, 15236 Athens, Greece*
[4]*Università di Bologna, Dipartimento di Astronomia, via Ranzani 1, 40127 Bologna, Italy*
[5]*Departamento de Ciencias Fisicas, Universidad Andres Bello, Av. Republica 252, Santiago, Chile*
[6]*Max-Planck-Institut für Plasmaphysik and Excellence Cluster Universe, Boltzmannstrasse 2, D-85748 Garching, Germany*
[7]*Max-Planck-Institut für Extraterrestrische Physik, Giessenbachstrasse 1, D-85748 Garching, Germany*
[8]*Instituto de Astronomía, Universidad Nacional Autonoma de Mexico, Ensenada, Baja California, Mexico*
[9]*Osservatorio Astronomico di Roma (INAF), Via Frascati 33, I-00040 Monte Porzio Catone, Italy*
[10]*SSAI, Lanham, MD 20706, USA*
[11]*Observational Cosmology Laboratory, Code 665, Goddard Space Flight Center, Greenbelt, MD 20771, USA*

Accepted 2012 August 6. Received 2012 August 6; in original form 2012 April 27

ABSTRACT

In this paper we investigate the power spectrum of the unresolved 0.5–2 keV cosmic X-ray background (CXB) with deep *Chandra* 4-Msec (Ms) observations in the *Chandra Deep Field* South (CDFS). We measured a signal that, on scales >30 arcsec, is significantly higher than the shot noise and is increasing with angular scale. We interpreted this signal as the joint contribution of clustered undetected sources like active galactic nuclei (AGN), galaxies and the intergalactic medium (IGM). The power of unresolved cosmic source fluctuations accounts for ∼12 per cent of the 0.5–2 keV extragalactic CXB. Overall, our modelling predicts that ∼20 per cent of the unresolved CXB flux is produced by low-luminosity AGN, ∼25 per cent by galaxies and ∼55 per cent by the IGM. We do not find any direct evidence of the so-called 'warm hot intergalactic medium' (i.e. matter with $10^5 < T < 10^7$ K and density contrast $\delta < 1000$), but we estimated that it could produce about 1/7 of the unresolved CXB. We placed an upper limit on the space density of postulated X-ray-emitting early black holes at $z > 7.5$ and compared it with supermassive black hole evolution models.

Key words: galaxies: active – dark matter – diffuse radiation – large-scale structure of Universe – X-rays: galaxies.

1 INTRODUCTION

The cosmic X-ray background (CXB) is the result of a multitude of energetic phenomena occurring in the Universe since the epoch of formation of the first galaxies. Its nature has been investigated in the last 50 yr with several telescopes but only in the 1980s did it become clear that its main contributors are active galactic nuclei (AGN) (Setti & Woltjer 1989). Later it was found that galaxies, galaxy clusters, large-scale structures and diffuse hot gas in the Milky Way are also sources contributing to the CXB (Fabian & Barcons 1992).

With the launch of *ROSAT*, *Chandra* and *XMM–Newton*, our knowledge regarding the nature of sources contributing to the flux of the CXB became suddenly clearer. Deep surveys like the *Chandra Deep Fields* South (CDFS: Giacconi et al. 2001; Luo et al. 2008; Xue et al. 2011) and North (CDFN: Brandt et al. 2001) and the Lockman Hole (Brunner et al. 2008) have almost conclusively resolved the problem of the CXB below 10 keV. In fact, at the flux limits of *Chandra* and *XMM–Newton*, about 90–95 per cent (Moretti et al. 2003; Bauer et al. 2004; Lehmer et al. 2012) of the 0.5–2 keV CXB flux has been resolved[1] into point and extended sources.

CXB synthesis models (see e.g. Treister & Urry 2006; Gilli, Comastri & Hasinger 2007) predict that at fluxes fainter that the

[1] In these papers, the fraction of unresolved CXB has been estimated at the flux of the faintest detected source; here we measure the average value for the investigated area.

★E-mail: nico.cappelluti@oabo.inaf.it

© 2012 The Authors
Monthly Notices of the Royal Astronomical Society © 2012 RAS

Downloaded from http://mnras.oxfordjournals.org/ at NASA Goddard Space Flight Ctr on July 14, 2014

current limits the AGN source counts progressively flatten and then galaxies become the more abundant sources.

Galaxies emerge as the dominant population at faint 0.5–2 keV fluxes, with a break-even point at around $\sim 10^{-17}$ erg cm^{-2} s^{-1} (see also Lehmer et al. 2007; Xue et al. 2011; Lehmer et al. 2012) and can make up a sizeable fraction of the X-ray background (9–16 per cent: Ranalli, Comastri & Setti 2005). The contribution from galaxy clusters, down to a mass limit of $\sim 10^{13}$ M$_\odot$, has been estimated to be of the order of $\sim$10 per cent of the total 0.5–2 keV CXB (Gilli, Risaliti & Salvati 1999; Lemze, Sadeh & Rephaeli 2009).

Several authors studied the clustering properties of the CXB to unveil the nature of the sources producing its flux and their properties (Martin-Mirones et al. 1991; Wu & Anderson 1992; Sołtan & Hasinger 1994; Barcons, Fabian & Carrera 1998). The most used technique is that of the two-point autocorrelation function of the surface brightness of the CXB. While at the time of *HEAO-1* the task was to determine the contribution of quasi-stellar objects (QSOs) to the CXB, since *ROSAT* most of the investigations in this field have been performed to unveil signatures of the warm hot intergalactic medium (Sołtan, Freyberg & Hasinger 2002; Sołtan 2006; Galeazzi, Gupta & Ursino 2009) and to test cosmological models (Diego et al. 2003). This kind of study is therefore extremely powerful to study the populations of sources that are beyond the resolving and detection capabilities of our instruments.

In the Great Observatories Origins Deep Survey (GOODS) fields, Hickox & Markevitch (2006, 2007) have shown that, after excising detected point and extended sources plus faint *HST* detected galaxies, the spectrum of the soft CXB still shows a signal in the 0.5–2 keV band. While a large fraction of it could be attributed to a local component (solar-wind charge exchange and Milky Way thermal emission), they showed that below 1 keV the fraction of resolved CXB is not sensitive to the removal of *HST* galaxies, thus arguing for a purely diffuse nature of the unresolved CXB. In the 1–2 keV band they have shown that, by removing *HST* source areas from the analysis, the fraction of unresolved CXB drops by $\sim$50 per cent. This means that a large fraction of the unresolved 1–2 keV CXB flux could be produced in faint undetected galaxies (active or non-active). Moreover, they speculated that a large fraction of the unresolved CXB may be due to faint 3.6-μm Infrared Array Camera (IRAC) sources, suggesting that high-z or absorbed sources could produce a large part of such radiation. According to their estimate, the remaining fraction of the CXB (i.e. 2–3 per cent of the 0.5–2 keV CXB) remains consistent with the prediction of warm hot intracluster medium (WHIM) intensity from hydrodynamical simulations (see e.g. Cen & Ostriker 1999; Ursino & Galeazzi 2006; Roncarelli et al. 2006, 2012).

In the local Universe about 30–40 per cent of the baryons are missing with respect to what is measured at $z \sim 3$ (Fukugita, Hogan & Peebles 1998). Simulations predict that most of these baryons were shock-heated and at $z \lesssim 1$ they should have a temperature of the order 10^5–10^7 K and therefore emit thermal X-rays (Cen & Ostriker 1999). Controversial evidence on the properties of such a medium has been published so far (see e.g. Nicastro et al. 2005; Kaastra et al. 2006; Fang et al. 2010; Shull, Smith & Danforth 2012). Although it has very low surface brightness,the WHIM can be distinguished from other kinds of diffuse emission on the basis of its clustering properties (Ursino & Galeazzi 2006). In fact, its emission follows that of clusters and filaments and peaks at low redshift ($z \sim 0.5$), thus showing a typical feature in the angular clustering of unresolved CXB fluctuations. However, the WHIM is not the only expected component of the unresolved CXB arising from thermal emission of the intergalactic medium (IGM). X-ray surveys in the local Universe revealed X-ray emission from local galaxy groups down to masses of the order of 10^{12} M$_\odot$ (see e.g. Eckmiller, Hudson & Reiprich 2011). Since the intensity of the X-ray emission of galaxy groups scales with their mass, a large number of them were not detected at moderately high z. Therefore we also expect a contribution to the overall signal from medium- to low-mass groups at $z > 0.2$–0.3.

Concerning the unresolved extragalactic CXB, it is difficult to distinguish its components with a simple spectral analysis, mostly because of the poor energy resolution of X-ray-sensitive CCDs (i.e. $\sim$130 eV for ACIS-I at 1.5 keV). However, cosmological sources leave a unique imprint in the power spectrum (PS) of the anisotropies of the fluctuations of the unresolved CXB in a way that is related to their clustering and volume emissivity properties.

The unresolved CXB contains information about all those sources that have not been detected at the deepest fluxes reachable by deep surveys. Moreover, the amplitude of the PS is not only sensitive to the luminosity density of those sources but also provides information about their bias.

In this paper we study the power spectrum of the unresolved 0.5–2 keV CXB with 4-Ms CDFS data, the deepest X-ray observation ever performed to date. We model the anisotropies of the unresolved CXB with state-of-the art results on galaxy and AGN evolution models and observations as well as with modern hydrodynamical cosmological simulations.

Throughout this paper we will adopt a concordance ΛCDM cosmology with $\Omega_{\rm m} = 0.3$, $\Omega_\Lambda = 0.7$, $H_0 = 70\,h$ km s^{-1} Mpc^{-1} and $\sigma_8 = 0.83$. Unless otherwise stated, errors are quoted at 1σ level and fluxes refer to the 0.5–2 keV band. We used as reference cumulative 0.5–2 keV CXB flux the recent estimates of Lehmer et al. (2012), $S_{\rm CXB}(0.5\text{–}2) = 8.15 \pm 0.58 \times 10^{-12}$ erg cm^{-2} s^{-1} deg^{-2}.

2 DATA SET

For the purposes of this work we used the 4-Ms *Chandra* exposure on the CDFS (Xue et al. 2011). This is the deepest *Chandra* observation ever performed and reaches a point-source flux limit of $\sim 10^{-17}$ erg cm^{-2} s^{-1}. A detailed description of the data reduction and catalogue production is given in Xue et al. (2011). In order to improve the sensitivity for extended sources, we also used the 3-Ms *XMM–Newton* exposure in the same field (Ranalli et al., in preparation). Since the scope of this paper is to measure the angular PS (see next section) of the purely diffuse, unresolved CXB, we masked the *Chandra* data from all point sources detected by Xue et al. (2011). The combination of the *Chandra* and *XMM–Newton* observations allowed us also to remove, with unprecedented sensitivity, extended sources down to 0.5–2 keV fluxes of 2×10^{-16} erg cm^{-2} s^{-1} (Finoguenov et al., private communication). In order to employ the area with best point spread function (PSF), we limited our analysis to the inner 5 arcmin from the exposure-weighted mean optical axis ($\alpha = 03^{\rm h}32^{\rm m}27\overset{\rm s}{.}316$, $\delta = -27^\circ 48' 50\overset{''}{.}36$). Point sources have been masked with circular regions of 5-arcsec radius (which is large enough to mask >99 per cent of the source flux at every off-axis angle investigated here) and extended sources have been masked out to R_{200} (i.e. the radius within which the matter overdensity is >200). In this way the remaining counts on the detector are made, to a good approximation, by particle background and purely diffuse cosmic background only. With such a masking our image contains 163 940 counts, with an average occupation number of 1.7 count pixel^{-1}. The total investigated masked area (80.3 arcmin^2) is shown in Fig. 1, together with the raw image of the same region. The source masking removes a fraction of the useful area of

Downloaded from http://mnras.oxfordjournals.org/ at NASA Goddard Space Flight Ctr on July 14, 2014

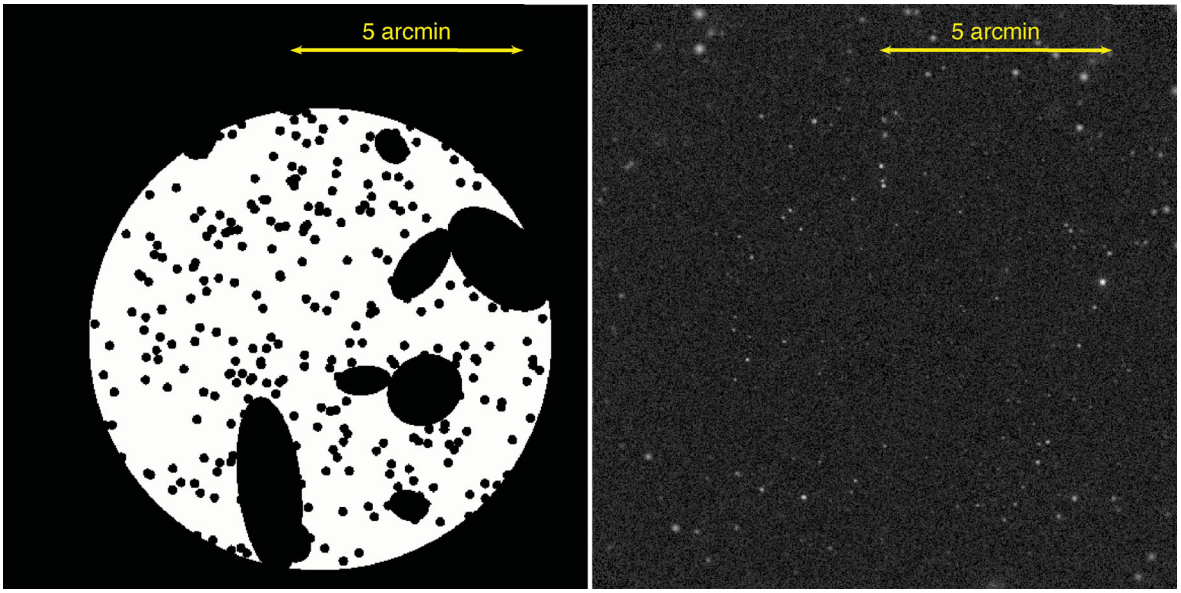

Figure 1. Left: the mask adopted for the ACF analysis in the observations of the CDFS. The white area is the resulting source-free area. Right: 0.5–2 keV image of the same area smoothed with a Gaussian filter with 3 arcsec width.

about ∼25 per cent and therefore the source-free area is of the order of 60 arcmin^2. In principle the evaluation of the PS should not change if we increase the size of the mask. However, by increasing the mask size we would run into an overmasking problem that would bias the estimate of the PS. If the masking were larger than ∼30–40 per cent of the active pixels then the PS analysis would have been biased by the mask (Kashlinsky et al. 2012). A smaller size of mask would increase the overall power, since it would be polluted by the power from cluster outskirts and PSF tails of detected sources. In order to improve the signal-to-noise ratio of the weak signal we are looking for, we applied a careful filtering of the background. We have additionally filtered the events files provided by the *Chandra* X-ray Center (CXC) from particle flares by using the CIAO routine `lc_clean`.[2] Such a technique is more sensitive than the classical procedures adopted in standard pipelines. In order to reduce the noise introduced by low-count statistics, images were binned in pixels of 1.5 arcsec size. Images have been produced in the 0.5–2 keV energy range, where *Chandra* has the largest collecting area and detector efficiency.

3 EVALUATION OF THE POWER SPECTRUM

In order to estimate the power spectrum we adopt the method described in Arevalo et al. (2012) and Churazov et al. (2012), which has been developed with the purpose of estimating the PS of 2D images with gaps. Here we give a brief description of the technique used to evaluate the PS, but we refer the reader to Arevalo et al. (2012) for a more comprehensive description.

The first step is to derive the fluctuation field at any given angular scale θ, from which we derive a low-resolution PS by using a Mexican-Hat (MH) filter,

$$F(x) = \left[1 - \frac{x^2}{\theta^2}\right] \mathrm{e}^{-x^2/(2\theta^2)}.$$

The goal is to single out fluctuations at any given angular scale and then compute the variance of the fluctuation field image, $\delta_S^2(k)$. Our map has gaps introduced by features in the exposure maps and by the mask. The mask (M) is an image having value $M = 0$ in the region of excised sources and $M = 1$ elsewhere. The method corrects for gaps by representing the MH filter as a difference between two Gaussian filters with slightly different widths, convolving the image and the mask with these filters and dividing the results before calculating the final filtered images. It has been shown (Arevalo et al. 2012) with numerical simulations that this method also takes data masking efficiently into account when a large fraction of the field is masked and, independently of the mask shape, the normalization and shape of the PS are accurately estimated. At any given frequency $k = 1/\theta$, we estimated the PS of the fluctuation field as follows.

We define the fluctuation image at the scale θ as

$$I_\theta = M \times \left[\frac{G_{\theta_1} \circ (I)}{G_{\theta_1} \circ M} - \frac{G_{\theta_2} \circ (I)}{G_{\theta_2} \circ M}\right], \quad (1)$$

where ($G_{\theta_1} \circ I$, $G_{\theta_2} \circ I$) represent the count-rate image (I) convolved with Gaussian filters with widths $\theta_{1,2}(G)$ and M is the mask.[3] The width of the filter is chosen as $\theta_1 = \theta\sqrt{1+\epsilon}$ and $\theta_2 = \theta/\sqrt{1+\epsilon}$, where $\epsilon \ll 1$. In this way the value in the brackets of equation (1) is dominated by fluctuations at scale $\sim\theta$.

Arevalo et al. (2012) demonstrated that the PS of the fluctuation field at frequency $k = 1/\theta$ [$P_2(k)$] is related to the variance of the image via

$$P_2(k) = \frac{1}{\epsilon^2 \pi k^2}\sigma^2(I_\theta) = \left\langle |\delta_S(k)|^2 \right\rangle. \quad (2)$$

In this work we used $\epsilon = 0.1$, however a different value of ϵ does not change the estimate of the PS provided that $\epsilon \ll 1$. Note that in the calculation of the variance we have made no assumption on the distribution of the fluctuation amplitude; thus the method also works in the Poisson regime. This method is equivalent to classical Fourier analysis; the only difference is that this treatment of gaps and choice of filters allows us to retrieve the underlying power-spectrum regardless of the shape of the mask. Unless otherwise stated, errors are given at the 1σ level. In Fourier analysis, the uncertainty in

[2] http://cxc.harvard.edu/ciao/ahelp/lc_clean.html

[3] The symbol ∘ stands for convolution.

Downloaded from http://mnras.oxfordjournals.org/ at NASA Goddard Space Flight Ctr on July 14, 2014

the power estimate is solely related to the accuracy with which one can estimate the variance. At every frequency, this depends on the number of independent elements in Fourier space and the intrinsic dispersion of the data. In our analysis, since we adopt a broad filter, we need to define at every frequency k the mean number of real Fourier elements used to evaluate the amplitude of the fluctuations $\langle N_k \rangle$. In principle the uncertainties can be approximated with $\sigma_P(k) \approx P_2(k)/\sqrt{0.5\langle N_k \rangle}$. Following the extensive description of Arevalo et al. (2012), within our formulation errors are computed with

$$\sigma_P(k) = \frac{\sqrt{\int_q (P(k)\, F_{qx}^2\, \mathrm{d}q}}{F_{kx}^2} \frac{N}{N_{M=1}}, \tag{3}$$

where F_{kx} is the Fourier transform of the filter, N is the total number of pixels and $N_{M=1}$ is the number of unmasked pixels.

These filter-weighted expected uncertainties are what we plot as error bars.

Power-spectrum points measured in this way are partially dependent on their neighbour frequencies as a result of the finite width of the power filter. Therefore, points can only be considered independent if they are measured at spatial scales that are sufficiently separated. In our case, where we used a factor of 2 separation in angular scale, it is appropriate to use PS estimates and errors as independent points in the usual fitting methods.

4 RESULTS

4.1 Baseline method

The power spectrum estimated with the technique described is Section 3 is shown in Fig. 2. We computed the probability that the observed data could be produced by a statistical fluctuation of a zero-power signal by using a simple χ^2 test. We obtained a value of $\chi^2 = 140$, corresponding to a $>10\sigma$ significance with respect to zero power. The high-frequency part is dominated by a white-noise component, while the signal increases towards lower frequencies (i.e. large scales). In *Chandra* images, a large fraction of the fluctuation can be attributed to Poisson noise due to the low-count statistics.

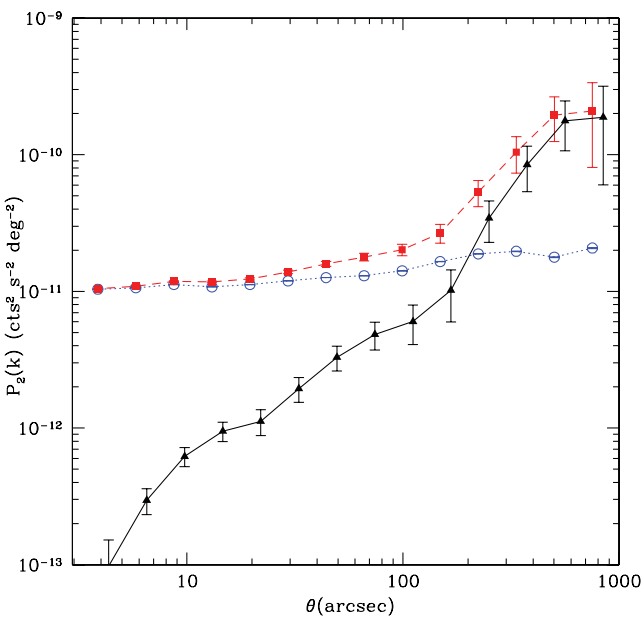

Figure 2. Squares (red in the online article): the raw PS of the source-masked fluctuations of the CXB as a function of the angular scale. Open circles (blue in the online article): the (A-B)/2 PS. Black triangles: the resulting cosmic PS after subtracting the 'spurious' power. Black symbols are artificially shifted for sake of clarity.

We estimated $P_{\rm noise}$ directly from the data by using the $A - B$ technique (Kashlinsky et al. 2005). For every pointing we sorted the events in order of time arrival and created two images, one including even events (A) and the other with odd events (B). We have then mosaicked all the A and B images. In this way we have two identical images with half the photons with respect to the full data set, both having the same exposure and thus containing the same information on the signal but with their own noise. Any systematic errors should be manifested very similarly in the A and B images and thus the $(A - B)/2$ difference images provide a useful means of characterizing the random (noise) properties of the data sets. The PS of the difference image $(A - B)/2$ is therefore nothing other than the PS of fluctuations due to Poisson noise. Source variability does not affect this procedure, since the sampling of their light curve does not change significantly: the gap between two consecutive events is of the order of the read-out time of the detector, which is much shorter than the typical variability of X-ray sources. In Fig. 2 we show the PS of the Poisson noise compared with the PS of the raw image. As expected, the Poisson noise shows a flat (white noise) spectrum. Throughout this paper we assume that both particle and galactic background contribute only to the Poisson noise, since their flux is expected to be homogeneous at the scales sampled by this investigation. The total cosmic PS ($P_{2,\rm CXB}$) is therefore obtained with

$$P_{2,\rm CXB} = P_{2,\rm tot} - P_{2,(A-B)/2}. \tag{4}$$

The estimated $P_{2,\rm CXB}$ is plotted in Fig. 2. In the angular range sampled here ($3\,\mathrm{arcsec} < \theta < 1000\,\mathrm{arcsec}$), the power increases with scale, becoming close to zero at the smallest scale. The errors in $P_{2,\rm CXB}$ have been obtained by propagating the errors of $P_{2,\rm tot}$ and $P_{2,(A-B)/2}$.

5 MODELLING THE CXB ANISOTROPIES

In order to interpret the cosmic signal measured in the PS of the CXB, we used population synthesis models and recent observational results to predict the amplitude and shape of its components. We want to test the assumption that the total observed fluctuations can be reproduced by a simple three-source class model. Our hypothesis is that the amplitude and shape of the PS are produced by shot noise from individual undetected AGN and galaxies within the instrument beam (discrete source counts), clustering of galaxies and AGN below the limiting flux and clustering of undetected diffuse hot cosmological gas in large-scale structures (IGM, i.e. undetected groups and WHIM filaments). We then test the statistical robustness of our hypothesis with a χ^2 test, where every component is considered as a parameter. In addition we provide an upper limit for the still undetected high-z sources. We assumed that, on the angular scales investigated here, fluctuations from the Milky Way diffuse emission do not contribute to the PS, i.e. this emission can be described as a constant flux on the detector and therefore is contributing to the Poisson noise only. This hypothesis is supported by PS measurements of the soft CXB with *ROSAT* (Śliwa, Soltan & Freyberg 2001), which show that the Galaxy produces a signal only for the smallest harmonics of the PS. Moreover, cosmological sources (AGN, galaxies and IGM) partially share the same environment; thus we include in the model a cross-power term to model the

Downloaded from http://mnras.oxfordjournals.org/ at NASA Goddard Space Flight Ctr on July 14, 2014

amplification of fluctuations produced by their cross-correlation. In summary, the CXB PS can be modelled as

$$P_{2,\mathrm{CXB}}(k) = P_{2,\mathrm{SN}}(k) + P_{2,\mathrm{AGN}}(k) + P_{2,\mathrm{GAL}}(k) + P_{2,\mathrm{IGM}}(k) + P_{2,\mathrm{A,G,I}}(k), \quad (5)$$

where $P_{2,\mathrm{SN}}(k)$, $P_{2,\mathrm{AGN}}(k)$, $P_{2,\mathrm{GAL}}(k)$ and $P_{2,\mathrm{IGM}}(k)$ are the PS of shot noise and the clustering components of AGN, galaxies and IGM, respectively. $P_{2,\mathrm{A,G,I}}(k)$ is the cross-power term, which contains the cross-correlation of AGN and galaxies, AGN and IGM and galaxies and AGN, respectively. In the following sections we will describe the procedure adopted to model each spectral component.

5.1 Preliminaries

To decompose $P_{2,\mathrm{CXB}}$ into its primary components we adopt the procedure described by Kashlinsky (2005). Whenever a fraction of the sky of order $\theta < 1$ rad is concerned, one adopts the Cartesian formulation for Fourier analysis. The fluctuation field of the CXB surface brightness (S) is defined as $\delta S = S(\theta) - \langle S \rangle$. $P_2(k)$ is related to the auto-correlation function $C(\theta)$ through

$$P_2(k) = \int_0^\infty C(\theta) J_0(k\theta) k \, \mathrm{d}k, \quad (6)$$

where $J_0(x)$ is the zeroth-order cylindrical Bessel function. A very useful quantity is the mean-square fluctuation within a finite beam of angular radius θ, or zero-lag correlation, which is related to the PS via

$$C(0) = \langle \delta S^2 \rangle_\theta = \frac{1}{2\pi} \int_0^\infty P_2(k) W_{\mathrm{TH}}(k\theta) k \, \mathrm{d}k \propto k^2 P_2(k), \quad (7)$$

where W_{TH} is the window function. Thus, in order to visualize the relative strength of the fluctuations at any given scale $1/k$, a useful quantity is $\sqrt{k^2 P_2(k)}$, which differs from the actual value of $\langle \delta_S \rangle_\theta$ by a factor of order unity that depends on the window function.

5.2 Shot-noise level and PSF modelling

The shot noise is produced by discrete sources in the beam. The relative amplitude of this component scales as $N^{-1/2}$, where N is the mean number of sources entering the beam. $P_{2,\mathrm{SN}}$ is therefore very important in surveys performed by instruments with high angular resolutions like *Chandra*. If sources are removed down to a flux S_{lim}, it can be shown (Kashlinsky 2005) that the shot-noise component can be expressed as

$$P_{2,\mathrm{SN}} = \int_0^{S_{\mathrm{lim}}} S^2 \frac{\mathrm{d}N_{\mathrm{X}}}{\mathrm{d}S} \, \mathrm{d}S, \quad (8)$$

where $\mathrm{d}N_{\mathrm{X}}/\mathrm{d}S$ is the differential $\log N - \log S$ of all the X-ray point sources (i.e. AGN, galaxies, stars). In most cases, the sensitivity of the survey is not homogeneous across the field of view. This means that S_{lim} in equation (8) is a function of the sky coordinates. To account for this selection effect, we scaled the number counts by the selection function computed as follows: we computed the sensitivity map of the surveyed area by imposing the same false source detection rate adopted by Xue et al. (2011) for catalogue production (i.e. $P_{\mathrm{false}} < 0.004$). By using the masked maps described above, we estimated the minimum count rate necessary not to exceed the threshold mentioned above.

In Fig. 3 we show the selection function in terms of fraction of field of view as a function of the flux limits. If $\eta(S)$ is the selection function for sources with flux S, the source counts of sources producing the shot noise are given by

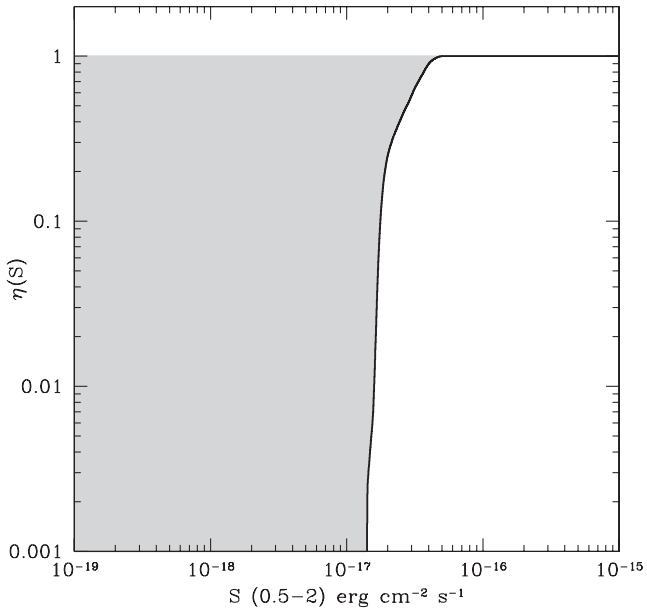

Figure 3. Black line: the selection function for point sources in the inner 5 arcmin of the 4-Ms CDFS. The grey shaded area represents the complement of the selection function ($1 - \eta(S)$), highlighting the flux region from where the fluctuations are produced.

$$\left.\frac{\mathrm{d}N_{\mathrm{X}}}{\mathrm{d}S}\right|_{(\mathrm{SN})} = \alpha \, [1 - \eta(S)] \, \frac{\mathrm{d}N_{\mathrm{X}}}{\mathrm{d}S}. \quad (9)$$

Here α is a factor that accounts for the lower normalization observed in the CDFS with respect to larger area fields and with the Gilli et al. (2007) model (Cappelluti et al. 2009). We measured α by comparing the Lehmer et al. (2012) 0.5–2 keV $\log N - \log S$ and the Gilli et al. (2007) modelled $\log N - \log S$ at the break flux and obtained $\alpha = 0.72$. We fixed the level of shot noise in our data by computing the integral in equation (8), by assuming that the only sources accounting for shot noise are AGN and galaxies. Therefore in this case we adopt

$$\left.\frac{\mathrm{d}N_{\mathrm{X}}}{\mathrm{d}S}\right|_{\mathrm{SN}} = \left.\frac{\mathrm{d}N_{\mathrm{X}}}{\mathrm{d}S}\right|_{\mathrm{AGN}} + \left.\frac{\mathrm{d}N_{\mathrm{X}}}{\mathrm{d}S}\right|_{\mathrm{Gal}}. \quad (10)$$

$\mathrm{d}N/\mathrm{d}S_{\mathrm{AGN}}$ has been estimated from the population synthesis model of Gilli et al. (2007) and $\mathrm{d}N/\mathrm{d}S_{\mathrm{Gal}}$ has been computed with the model of X-ray galaxy evolution described in Section 5.4. In our calculations, fluxes have been converted into count rates by assuming an average power-law spectrum with spectral index $\Gamma = 1.7$. With such an assumption, count rates are obtained by multiplying the flux by an energy conversion factor $\mathrm{ECF} = 1.66 \times 10^{11}\ \mathrm{cm^2\,erg^{-1}}$. Note that a different choice of the spectral index of $\Delta\Gamma \sim \pm 0.3$ produces a 5 per cent variation of the ECF. The shot-noise PS is scale-independent (white noise) and since the signal from cosmological sources increases with scale, the contribution of $P_{2,\mathrm{SN}}$ to the total PS becomes more important at small angular scales.

According to these prescriptions, we obtained an estimate of $P_{\mathrm{SN}} = 1.58 \times 10^{-12}\ \mathrm{count^2\,s^{-2}\,deg^{-4}}$. The shot noise and also the other astronomical components of the PS are affected by instrument PSF. This effect consists of a multiplicative factor that applies to the effective PS. In order to model it, we used the empirical approach proposed by Churazov et al. (2012), where the PS of each modelled

Downloaded from http://mnras.oxfordjournals.org/ at NASA Goddard Space Flight Ctr on July 14, 2014

component is multiplied at every frequency by a factor

$$P_{\rm PSF}(k) = \frac{1}{[1+(k/0.12)^2]^{1.1}}, \quad (11)$$

where k is the angular frequency. In Fig. 6 (later) we show our estimate of $P_{\rm SN}$, taking into account the effects of the PSF. In comparison with the data, we find an excellent agreement of our estimated $P_{\rm SN}$ with the cosmic PS at short scales (i.e. $\theta < 20$ arcsec) and we interpret this as a confirmation of our assumptions. Note that after subtracting $P_{\rm SN}$ from $P_{2,\rm tot}(k)$, the remaining signal can be completely attributed to clustered sources and therefore to the sources contributing to the unresolved extragalactic CXB. In order to evaluate the strength of our detection, we computed the probability that our data could be obtained with a random fluctuation of a null flat signal. If we subtract the SN component at $\theta > 50$ arcsec we still observe a strong signal. In order to determine the significance of the remaining signal, we fitted our data, over the whole angular range, with a $P(k) = 0$ model (zero-power signal) to determine whether our signal could be due to a statistical fluctuation of a null signal. With such a model we obtained χ^2/d.o.f. = 43.5/13, thus rejecting our assumption at $>4\sigma$ confidence level. Since such a signal increases with scale, we interpret this as a clustered cosmic signal.

5.3 Anisotropies from AGN clustering

On the small angles sampled by our data, $P_{2,\rm CXB}$ is related to the unresolved CXB production rate, dS/dz, and the evolving 3D PS of the AGN, $P_{3,\rm AGN}(k)$, via Limber's equation (Peebles 1980). At any given redshift the PS of AGN can be related to the PS of matter by knowing their redshift-dependent linear biasing factor ($b(z)$: Kaiser 1984). Basically, we have

$$P_{3,\rm AGN}(k,z) = b(z)^2 P_{3,\rm M}(k,z), \quad (12)$$

where $P_{3,\rm M}(k,z)$, is the matter 3D PS. $P_{3,\rm M}(k,z)$ was estimated by using the CAMB[4] (Lewis & Bridle 2002) tool and including in the computation both linear and non-linear components of the matter PS (Smith et al. 2003). Although a large amount of work on galaxy and AGN clustering is present in the literature, here we choose to combine this cosmological tool with bias measurements and predictions because of the poor sampling of the redshift space of observations. The 2D PS can be then obtained with

$$P_{2,\rm AGN}(k) = \int_0^z \left(\alpha \frac{{\rm d}S}{{\rm d}z}\right)^2_{\rm AGN} \times \frac{P_{3,\rm AGN}(k[2\pi d_A * (1+z)]^{-1}, z)}{c\,{\rm d}t/{\rm d}z[d_A*(1+z)]^2} \frac{{\rm d}z}{1+z}, \quad (13)$$

where d_A is the angular diameter distance and the integration is performed in the redshift range $0 < z < 7.5$. A critical point of the analysis is the determination of the flux produced by undetected AGN at any given redshift. We derived dS/dz by using the CXB synthesis model published by Gilli et al. (2007). Briefly, the models take into account the observed luminosity function, k-corrections, absorption distribution and spectral shapes (see Gilli et al. 2007 for more details) of AGN and returns the observed flux at any given redshift, using

$$\frac{{\rm d}S}{{\rm d}z} = \int_0^\infty [1-\eta(S)] \int_z^{z+{\rm d}z} \frac{L'}{4\pi d_L^2}\,\phi(L',z)\,\frac{{\rm d}V}{{\rm d}z}\,{\rm d}L'\,{\rm d}z, \quad (14)$$

where d_L is the luminosity distance, L' is the luminosity measured in the $0.5(1+z) - 2(1+z)$ keV range and dV/dz is the comoving volume element. The values of dS/dz have been calculated with the interactive tool provided by Gilli et al. (2007).[5] The population of AGN used to compute the 0.5–2 keV CXB production rate has the following properties: $42 < \log(L_{\rm X}) < 47$ erg s^{-1}, $20 < \log(N_{\rm H}) < 26$ cm^{-2} and $0 < z < 7.5$. In addition, we included a high-redshift decline of the AGN space density (see e.g. Brusa et al. 2009; Civano et al. 2011). They indeed modelled the evolution of the AGN X-ray luminosity function (XLF) at $z > 2.7$ with an exponential decay ($\phi(L,z) = \phi(L,z_0) \times 10^{-0.43(z-z_0)}$ and $z_0 = 2.7$) on top of the expected extrapolation from the lower redshift parametrization of Hasinger, Miyaji & Schmidt (2005). In Fig. 4 we show the undetected AGN CXB production rate as a function of the redshift. The bulk of their flux contributing to the unresolved CXB comes from $z \sim 1$.

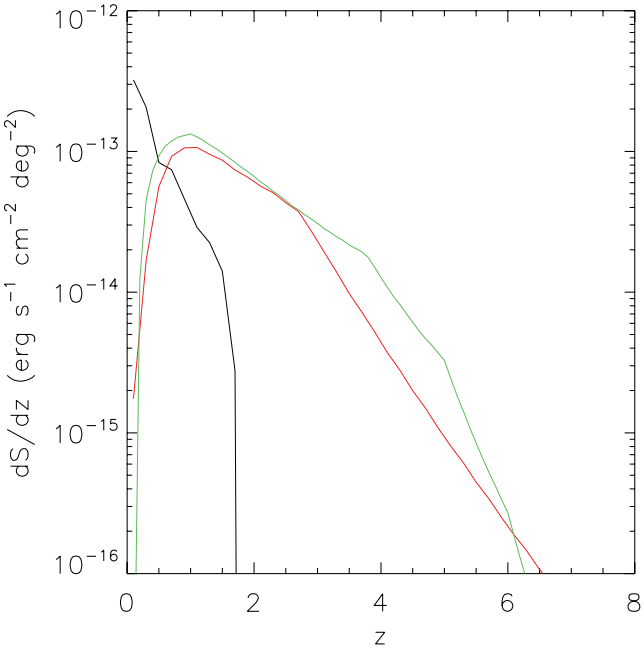

Figure 4. CXB production rate for undetected AGN (continuous line, red in the online article). Our prediction for the CXB production rate of undetected galaxies is also shown (green line in the online article). The black line represents emission from the IGM.

Another important ingredient in the computation of $P_{2,\rm AGN}(k)$ is the bias evolution of X-ray-selected AGN. It has recently become clear that below $z \sim 3$ AGN bias evolves like that of DM haloes (DMH) of mass $\sim 10^{13.1}$ M$_\odot$ (see e.g. Cappelluti, Allevato & Finoguenov 2012 for a review). However, at higher redshift the bias factor of X-ray AGN is still unknown, while for optically selected QSOs this has been modelled up to $z \sim 5$ (Hopkins et al. 2007; Bonoli et al. 2009; da Ângela et al. 2008) with quadratic polynomials. In Fig. 5 we compare the prediction of Bonoli et al. (2009), rescaled to fit the $z = 0$ X-ray-selected AGN bias, and the bias computed from analytical models (Sheth, Mo & Tormen 2001; van den Bosch 2002) for DMH with mass $\sim 10^{13.1}$ M$_\odot$. As one can see, both curves fit the observational data in an excellent way. Since the evolution at high z of the AGN bias factor is unknown and still a matter of debate, we assumed that the AGN bias evolves like the bias of DMH of mass $\sim 10^{13.1}$ M$_\odot$ up to $z \sim 10$. The contribution of AGN to the overall PS is shown in Fig. 6.

[4] http://camb.info/

[5] http://www.bo.astro.it/~gilli/counts.html

Downloaded from http://mnras.oxfordjournals.org/ at NASA Goddard Space Flight Ctr on July 14, 2014

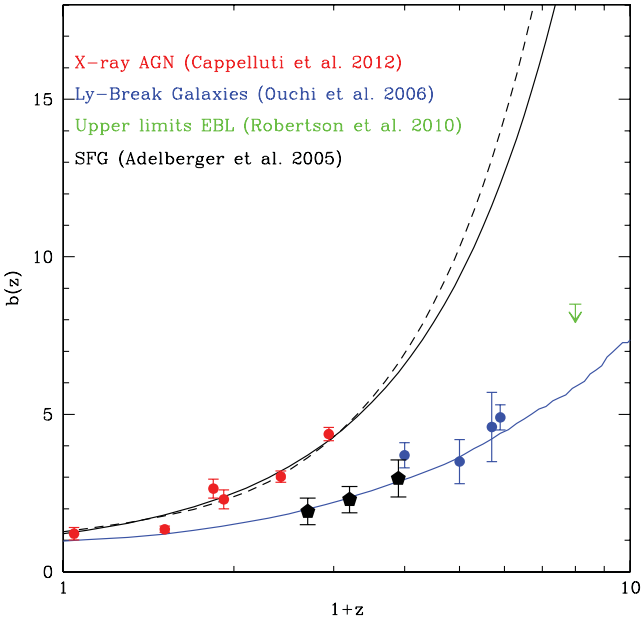

Figure 5. Black continuous line: bias evolution model adopted for AGN compared with data measured by Allevato et al. (2011) (dots, red in the online article). Black dashed line: bias evolution model for AGN of Bonoli et al. (2009). Lower line, blue in the online article: bias evolution model assumed for X-ray-emitting galaxies. Black pentagons: bias measurements for star-forming galaxies from Adelberger et al. (2005). Circles, blue in the online article: measurements of bias of high-z Lyman-break galaxies of Ouchi et al. (2004). The upper limit from EBL fluctuations of Robertson (2010) is shown in green in the online article.

5.4 Anisotropies from X-ray galaxy clustering

For anisotropies from galaxies we adopted a procedure similar to that used for AGN. The CXB production rate of galaxies[6] has been obtained by folding in equation (14) the $z = 0$ luminosity function measured by Ranalli et al. (2005) with the evolution measured for star-forming galaxies by Bouwens et al. (2011). The latter provides the most recent measurement of the evolution of star formation in the Universe up to $z \sim 10$ obtained with HST–WFC3. X-rays from non-active galaxies are mostly produced by low- and high-mass X-ray binaries. Such objects with X-ray luminosities of $\gtrsim 10^{37}$ erg s^{-1} cannot be detected individually in distant galaxies. The contributions from fainter discrete sources (including cataclysmic variables, active binaries, young stellar objects and supernova remnants) are well correlated with the star-formation rate of the galaxy itself. However, the ignition of X-ray activity in the stellar population of galaxies has a delay from the burst in star formation of the order of the time-scale of stellar evolution of the donor star in a binary system. Our model does not take into account effects of the delayed switch-on of X-ray binaries after star formation as was done by e.g Ptak et al. (2001); however, our representation allowed us to model the evolution of X-ray-emitting galaxies up to $z = 10$ with the most recent results on star-formation evolution.

As shown by Ranalli et al. (2005), the X-ray spectrum of galaxies can be represented by a simple power law with spectral index $\Gamma \sim 2$. With such an approximation no k-correction is needed.

In Fig. 4, we show the unresolved CXB production rate of galaxies as a function of the redshift. The contribution of galaxies to the total flux of the unresolved CXB is dominant with respect to AGN at $0 < z < 6.5$. Another parameter that enters into the determination of the contribution of galaxies to the X-ray PS is their bias factor and its evolution. Most of the modern galaxy-clustering analysis papers make use of the halo-occupation formalism and therefore it is not possible to derive an analytical formulation of the bias evolution. Moreover, galaxy clustering is complicated by the luminosity dependence of clustering (Ouchi et al. 2004). We therefore adopted a simple approximation for its determination, by assuming that the comoving correlation length of star-forming galaxies is constant, in the redshift range $0 < z < 7.5$, at the value measured by Adelberger et al. (2005) of $r_0 = 4.5\,\mathrm{Mpc}\,h^{-1}$ and their spatial correlation function can be modelled with a power law with $\gamma = 1.6$. Within this scenario the bias factor of galaxies can be estimated at every redshift via (Peebles 1980)

$$b(z) = \sigma_{8,\mathrm{G}}(z)/\sigma_{8,\mathrm{DM}}(z), \tag{15}$$

where $\sigma_{8,\mathrm{G}}(z)$ is the rms fluctuations of the galaxy distribution over a sphere with radius of 8 Mpc h^{-1} and $\sigma_{8,\mathrm{DM}}(z)$ is the same quantity for DM normalized to $\sigma_{8,\mathrm{DM}}(z = 0) = 0.83$. For such a power-law formalism it is possible to demonstrate that

$$(\sigma_{8,\mathrm{G}})^2 = J_2(\gamma)\left(\frac{r_0}{8\,\mathrm{Mpc}\,h^{-1}}\right)^{\gamma}, \tag{16}$$

where $J_2 = 72/[(3-\gamma)(4-\gamma)(6-\gamma)2^{\gamma}]$ (Peebles 1980). In Fig. 5 we compare our predicted bias evolution with the measurements of high-z Lyman-break galaxies of Ouchi et al. (2004) and with upper limits derived by Robertson (2010). As expected, galaxies are much less biased than AGN.

5.5 Emission from cosmological structures and WHIM

In the inset of Fig. 6 we show that, after including the contribution of the components mentioned above, the power spectrum still shows a prominent excess signal that, although with large error bars, increases up to a factor ∼3–4 toward low frequencies. Another significant contribution to the total signal of the CXB may arise from emission and clustering of unresolved galaxy clusters, groups and filaments. From the sensitivity maps of galaxy clusters we determined the flux limits for galaxy cluster/group detection and converted this into a luminosity limit at every redshift. For galaxy clusters and groups, luminosity, mass and temperature are related by scaling relations. The relations adopted here are discussed in Finoguenov et al. (2007). The luminosity limit can then be translated into a mass limit at every redshift. Thus our source detection ensures the removal of galaxy clusters and groups down to $\log(M) = 12.5$–$13.5\,\mathrm{M}_{\odot}$ (i.e. $kT < 1.5$ keV, see Fig. 7). Thus only the low-luminosity (low-mass) and warm population of galaxy groups contributes to the unresolved CXB. Since this class of objects is very difficult to model analytically, we describe their properties using a set of mock maps from Roncarelli et al. (2012), who used a cosmological hydrodynamical simulation to define the expected X-ray-surface brightness due to large-scale structures (LSS). The original hydrodynamical simulation (see the details in Tornatore et al. 2010) follows the evolution of a comoving volume of 37.5 h^{-1} Mpc^3 considering gravity, hydrodynamics, radiative cooling and a set of physical processes connected with the baryonic component, among which is a chemical enrichment recipe that allows us to follow the evolution of seven different metal species of the intergalactic medium (IGM). From its outputs, Roncarelli et al. (2012) simulated 20 light cones, covering the redshift interval $0 < z < 1.5$ with a size of ∼0.25 deg^2 (roughly 4 times the size of the CDFs) each

[6] We considered as 'galaxies' all those X-ray sources with $L_{\mathrm{X}}(0.5\text{–}2)\,\mathrm{keV} < 10^{42}$ erg s^{-1}.

Downloaded from http://mnras.oxfordjournals.org/ at NASA Goddard Space Flight Ctr on July 14, 2014

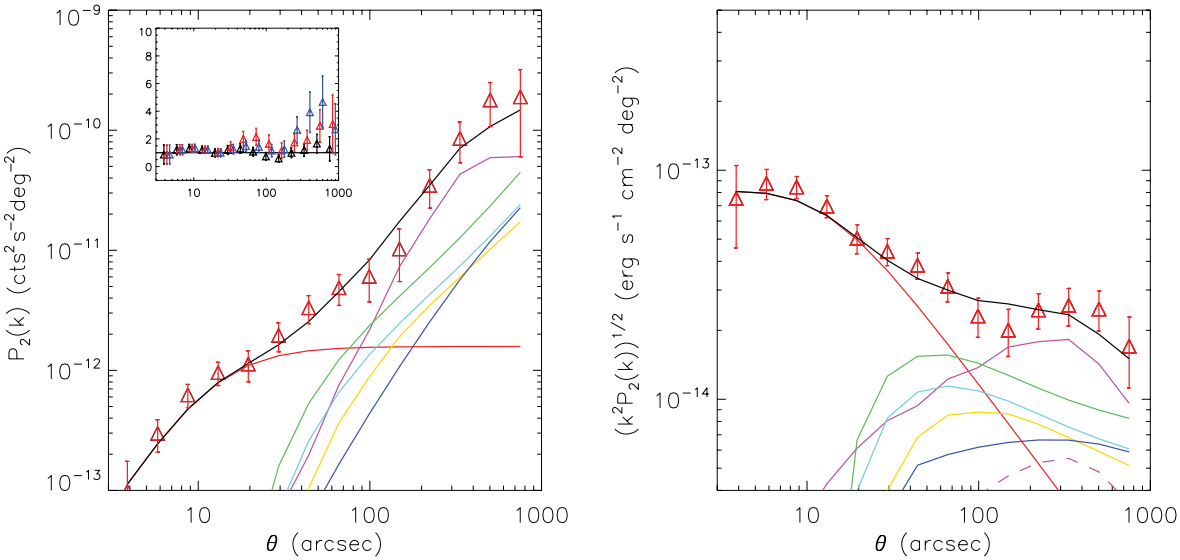

Figure 6. *Left panel.* Red triangles: cosmic PS in the CDFS as a function of the scale. Red continuous line: PS of the shot noise (galaxies and AGN). Green continuous line: PS of undetected AGN clustering. Cyan line: PS of undetected galaxy clustering. Magenta continuous line: total power from undetected hot gas in the IGM. Blue line: predicted clustering from of mini-quasars. The black line represents the overall model described in equation (5). The inset shows the data/model ratio as a function of scale for a SN and AGN+galaxy clustering model (blue), SN+IGM clustering model (red) and SN+AGN, galaxies and IGM clustering model (black). *Right panel.* Amplitude of the fluctuations as a function of angular scale with the same colour-coding as in the left panel with the addition of the contribution of IGM with $10^5 < T < 10^7$ K and overdensity $\delta < 1000$ following the classical definition of WHIM (magenta dashed line) to enhance its contribution to the total IGM flux. Yellow line: cross-correlation contribution.

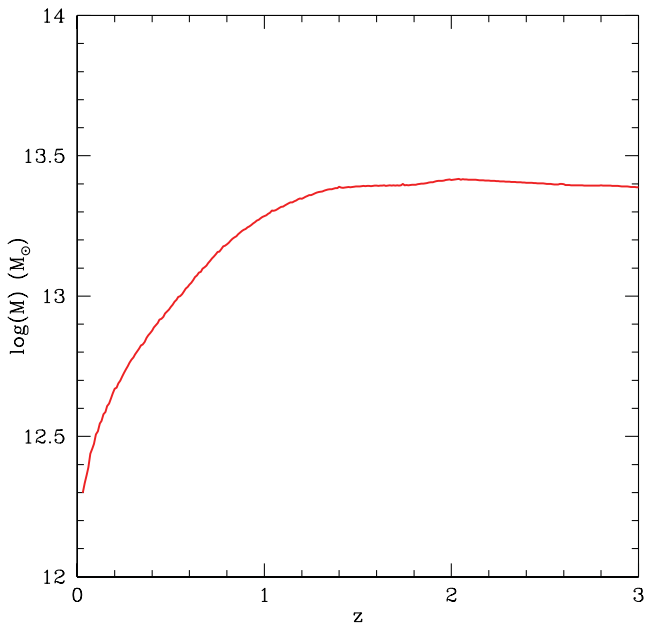

Figure 7. The line represents the lowest detectable mass in the 4-Ms CDFS as a function of redshift obtained through scaling relations.

and an angular resolution of 3.5 arcsec. Every pixel of the maps contains information about the expected observed spectrum in the 0.3–2.0 keV band with an energy resolution of 50 eV. The emission coming from the IGM was computed assuming emission from an optically thin collisionally ionized gas (`Apec` in XSPEC) model and considering the abundances of the different metal species provided by the simulation. These maps/spectra have been convolved with the *Chandra* response in order to reproduce the effective *Chandra* count rates. Since our data are masked for galaxy clusters, we applied to the simulations a source masking similar to that for the real data. The unresolved CXB production rate evaluated from simulations is shown in Fig. 4. We have simulated observations with the actual depth of the CDFS starting from the count-rate maps described above, folded through a flat exposure map. We have added an artificial isotropic particle and cosmic background according to the levels estimated by Hickox & Markevitch (2006, 2007). Random Poisson noise was artificially added to the image and we ran a simple sliding-cell detection with a signal-to-noise ratio threshold of 4. We have then excluded all the regions within which the overall encircled signal from sources is above 4σ with respect to the background. Since galaxy clusters and groups are highly biased, in order to smooth out the effects of sample variance we extracted the power spectrum from all the masked maps and averaged the results from all the realizations. Results of the PS modelling from the undetected IGM are shown in Fig. 6 (magenta solid lines). A long-standing debate in astrophysics is the possibility of detecting a signal in emission or in absorption from WHIM. In order to evaluate the contribution of WHIM to the overall PS signal of the unresolved CXB, we have extracted from our simulations the same light cones but including only all those photons with a temperature $10^5 < kT < 10^7$ K coming from regions with matter overdensity $\delta < 1000$. Such a selection is compliant with the classical definition of the WHIM, even if some denser clumps might also be present inside the filamentary structures [see the discussion in Roncarelli et al. (2012) and Fig. 8 for an example of the simulated structures]. We have masked the WHIM photon maps with the same masks used for clusters, extracted the PS and averaged over 20 realizations. The resulting modelled PS is shown in Fig. 6 (magenta dashed lines).

5.6 Cross-correlation terms

As mentioned above, AGN, galaxies and IGM partially share the same large-scale structures. For this reason, fluctuations are boosted by their cross-correlation term. The 3D cross-power spectrum (CPS)

Downloaded from http://mnras.oxfordjournals.org/ at NASA Goddard Space Flight Ctr on July 14, 2014

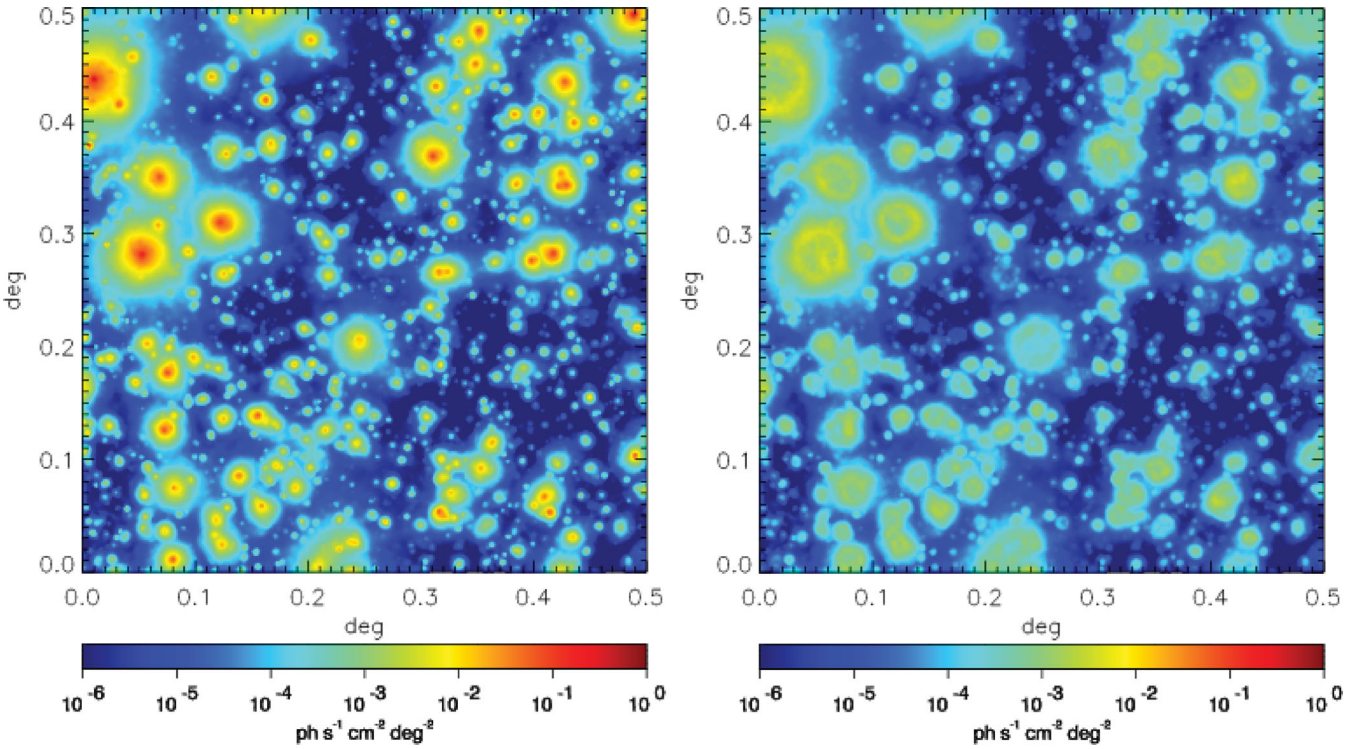

Figure 8. Left panel: whole simulation of the X-ray flux from cosmological structure. Right: the same but for the IGM with $10^5 < T < 10^7$ K and overdensity $\delta < 1000$.

of the source populations 1 and 2 is determined by

$$P_{3_{1,2}}(k) = b_1^2\, b_2^2\, P_{3,\mathrm{M}}(k, z), \tag{17}$$

where b_1 and b_2 are the bias factors relative to the source classes 1 and 2, respectively. In analogy with the PS, the angular CPS of diffuse emission produced by two populations with background production rates $\mathrm{d}S/\mathrm{d}z_1$ and $\mathrm{d}S/\mathrm{d}z_2$, respectively, can be evaluated with the following form of Limber's equation:

$$P_{2_{1,2}}(k) = \int_0^z \alpha^2 \left(\frac{\mathrm{d}S}{\mathrm{d}z}\right)_1 \left(\frac{\mathrm{d}S}{\mathrm{d}z}\right)_2 \times \frac{P_{3_{1,2}}(k[2\pi\, d_A * (1+z)]^{-1}, z)}{c\, \mathrm{d}t/\mathrm{d}z\, [d_A * (1+z)]^2}\, \frac{\mathrm{d}z}{1+z}. \tag{18}$$

We have then computed $P_{2_{\mathrm{AGN,IGM}}}$, $P_{2_{\mathrm{AGN,Gal}}}$ and $P_{2_{\mathrm{Gal,IGM}}}$ using the values of bias and emissivity described above. As far as the IGM is concerned, we adopted the bias evolution derived from simulations where $b_{\mathrm{IGM}}(z) = \sqrt{1+z}$. The overall cross-power term can be then expressed as

$$P_{2,\mathrm{A,G,I}} = P_{2_{\mathrm{AGN,IGM}}} + P_{2_{\mathrm{AGN,Gal}}} + P_{2_{\mathrm{Gal,IGM}}}. \tag{19}$$

The cross-power term is plotted in yellow in Fig. 6.

5.7 Accuracy of the PS model

Our CXB PS model is shown in Fig. 6, where it is compared with data. Here we summarize the ingredients adopted to model the PS components and their limits.

(i) At small separations most of the signal is due to shot noise produced by AGN and galaxies within the *Chandra* beam (red continuous line).

(ii) The AGN clustering is modelled by convolving the matter PS for a concordance ΛCDM cosmology, the AGN CXB production rate ($\mathrm{d}S/\mathrm{d}z$) derived from their X-ray luminosity function and a linear bias evolution of DMH of mass $\log(M) = 13.1\,\mathrm{M}_\odot$. Such a component increases with scale and its rms fluctuations (right panel) peak on scales of the order of 40–50 arcsec. Sources of uncertainties for such a component can be introduced by (a) our assumption on the bias evolution, which is unknown at $z > 2.5$, (b) the fact that evolution of the luminosity function has been determined at high z only for the most luminous sources and (c) the assumption at the basis of the Gilli et al. (2007) population-synthesis model. Fiore et al. (2012) suggest that low-luminosity AGN may show a milder evolution at high z with respect to observations at high luminosity. This may result in an underestimation of the power at large scales. However, as discussed above, the peak of the undetected CXB flux is produced by AGN at $z \sim 1.5$, where current observations are broadly consistent.

(iii) X-ray galaxy clustering (cyan line) is modelled by convolving the matter PS for a concordance ΛCDM cosmology, a model of the X-ray luminosity function obtained by assuming an evolution similar to that of star-forming galaxies starting from a measured $z = 0$ XLF and a linear bias evolution of sources having a correlation length $r_0 = 4.5\,\mathrm{Mpc}\,h^{-1}$. As for AGN, such a component increases with scale and its rms fluctuations peak (right panel) on scales of the order of 50 arcsec. The sources of uncertainties introduced by our models are, as in the case of AGN, twofold and basically driven by our choice of the bias and XLF evolution. In the X-ray band, the XLF of galaxies is known only up to $z \sim 1.5$, where it follows the evolution of star formation. The limit of our approach lies in the adopted model describing the cosmological evolution, which is however based on the reasonable assumption that X-ray galaxies

Downloaded from http://mnras.oxfordjournals.org/ at NASA Goddard Space Flight Ctr on July 14, 2014

trace star formation in the Universe. The same argument applies to bias, where no measurements have been performed in the X-ray band. However, also in this case, observational proxies are consistent with our assumptions at the redshift at which the bulk of the emission is produced, therefore limiting the margin of uncertainty of our modelling. Moreover, as we describe below, our modelling of the shot noise of AGN and galaxies is in good agreement with the data, meaning that our estimated source counts below the flux limit are statistically robust.

(iv) The diffuse gas contribution (magenta continuous line) is modelled by computing the PS of maps obtained by hydrodynamical cosmological simulations, which include a specific recipe of chemical enrichment. Sources detectable in real observations have been excised from these simulations before computing the PS. Such a component is responsible for most of the large-scale fluctuations that peak on a scale of a few arcmin. For comparison, we also evaluated the expected contribution of WHIM (magenta dashed line) to the overall fluctuations and found that, on the largest angular scales, it contributes up to ∼1/3 of the total power. The main source of uncertainty for this component definitely comes from the actual metallicity of the IGM in the lowest density phase, which has poor observational constraints. In addition, the largest scale clustering in the simulations may be underestimated because of the limited volume sampled in our cones.

In order to test our statistical hypothesis, we performed a χ^2 test and evaluated the improvement of the fit by adding one component after the other. We considered every component (which have their amplitude and shape fixed by our assumptions) as if they were a parameter of the fit for the evaluation of the degrees of freedom. The first test has been performed to evaluate whether the observed fluctuations could be explained by the shot-noise component only. As discussed above, such a hypothesis is rejected at $>4\sigma$ confidence level. Then we tested if, together with a shot-noise component, clustering of AGN and galaxies (including their cross-power) improved the fit. In this way we obtained χ^2/d.o.f. = 17.5/12. We also performed an F-test to evaluate the probability that the obtained χ^2 could be obtained by a statistical fluctuation of the SN-only model and obtained $P(F\text{-test}) = 1.2 \times 10^{-3}$; thus the inclusion of such a component significantly improves the fit. However, the relatively high χ^2/d.o.f. value suggests that additional or different components are required.

A visual inspection suggests that the strongest feature in the PS is produced by the IGM feature. Thus we fitted the data with a SN+IGM model and obtained χ^2/d.o.f. = 18.3/12, corresponding to $P(F\text{-test}) = 1.6 \times 10^{-3}$ with respect to the SN-only model. For such a model we show the data/model ratio in red in the inset of Fig. 6.

By adding the point-source clustering (and all the cross-power terms) to the latter model we obtain χ^2/d.o.f. = 7.8/11 and therefore the F-test, computed for the SN+IGM model, provides $P(F\text{-test}) = 2.7 \times 10^{-3}$, thus providing a further $\sim 3\sigma$ improvement of the fit. If we compare this fit with the SN-only model, the F-test probility is $P(F\text{-test}) = 7.9 \times 10^{-5}$, thus providing a significant improvement of the overall fit quality. The overall data/model ratio is shown in black in the inset of Fig. 6.

According to the values summarized in Table 1, we can safely confirm that the unresolved CXB in the CDFS can be explained with random and clustered signals from undetected point sources (AGN and galaxies), IGM clustering components plus a cross-correlation term.

6 FLUCTUATIONS FROM EARLY BLACK HOLES?

Potential contribution to the unresolved CXB and its structure can also come from very high redshifts overlapping with epochs usually identified with the era of the first stars. It is widely expected that fragmentation within the first collapsing protogalaxies was much less efficient, so that the first stars were significantly more massive and short-lived and could have left behind a non-negligible abundance of accreting black holes. Since, in addition, the first black holes could also have formed directly during the first-stars era, these populations may supply an additional, and potentially measurable, contribution to the unresolved CXB and its fluctuations.

Spitzer-based studies have revealed significant levels of source-subtracted cosmic infrared background (CIB) fluctuations, which were proposed to originate in the first-stars era (Kashlinsky et al. 2005). Indeed, the remaining known galaxy populations have been shown to produce significantly lower levels of CIB fluctuations (Helgason, Ricotti & Kashlinsky 2012) and there is no correlation in the large-scale structures between the *Spitzer* CIB maps at 3.6 and 4.5 μm and *HST*/ACS, likely pointing to the high-z origin of the excess CIB (Kashlinsky et al. 2007). The excess fluctuations have been confirmed in the AKARI-based analysis extending to 2.4 μm (Matsumoto et al. 2011) and the signal has now been measured to extend to $\sim 1^\circ$, exceeding the power over the remaining normal galaxies by well over an order of magnitude (Kashlinsky 2005). The level of the fluctuations at 3.6 μm is $\delta F_{\rm CIB} \sim 0.07\,{\rm nW\,m^{-2}\,sr^{-1}}$ and their energy spectrum appears to follow the Rayleigh–Jeans law, $\delta F_{\rm CIB} \propto \lambda^{-3}$, between 2.4 and 4.5 μm. If the excess CIB fluctuation arises at high z, the sources producing it would have a projected angular density of ∼(1–3) arcsec^{-2} (Kashlinsky et al. 2007). Under the assumption that the high-z sources measured by Kashlinsky et al. (2012) rapidly evolve into miniquasars (or early black holes), we estimated that, if the CIB/CXB flux ratio is constant over cosmic time, with a 3.6-μm extragalactic CIB flux of $\sim 6\,{\rm nW\,m^{-2}\,sr^{-1}}$ (Kashlinsky 2005) and extragalactic CXB flux of $8.15 \times 10^{-12}\,{\rm erg\,cm^{-2}\,s^{-1}\,deg^{-2}}$ (Lehmer et al. 2012), we obtain $S_{\rm CIB}/S_{\rm CXB} \sim 220$. Thus we evaluated the contribution to the CXB of the CIB fluctuations to be of the order $\sim 3 \times 10^{-13}/(1+z)\,{\rm erg\,cm^{-2}\,s^{-1}\,deg^{-2}}$ (i.e. ∼0.5 per cent of the CXB if these sources have $z \sim 7.5$–15).[7] We have therefore predicted the expected PS of these sources by folding their CXB production rate in equation (13) and integrating in the redshift range 7.5–15.

The result of this prediction is shown with a blue line in Fig. 6. A χ^2 fit of our five-component model provides χ^2/d.o.f = 8.3/10. Although the inclusion of such a component does not improve the quality of the fit, the statistics does not allow us to reject the hypothesis that these sources contribute to the observed fluctuations. These sources would contribute very weakly to the shot noise and the upper limit of their contribution is not larger than the uncertainty in the measured PS. Thus at 1σ we have $P_{\rm SN,mq} \lesssim 1 \times 10^{-13}\,{\rm count^2\,s^{-2}\,deg^{-4}}$ (i.e. the mean value of the uncertainty on those scales). According to equation (8), we can estimate the source density of putative miniquasars with $P_{\rm SN}/S_{\rm min}^2 \sim N(>S_{\rm min})$. If $S_{\rm min} = 10^{-20}\,{\rm erg\,cm^{-2}\,s^{-1}}$, where most CXB models predict the saturation of the source counts, we estimate $N \lesssim 60.000\,{\rm deg^{-2}}$. If these sources shine in the redshift range 7.5–15 (Kashlinsky et al. 2012), then their comoving volume density is $\leq 9 \times 10^{-5}\,{\rm Mpc^{-3}}$. For comparison, in the same redshift range the Gilli et al. (2007)

[7] Assuming $b(z) = \sqrt{1+z}$.

Downloaded from http://mnras.oxfordjournals.org/ at NASA Goddard Space Flight Ctr on July 14, 2014

model predicts, for X-ray-selected AGN, in the luminosity range sampled by our fluctuations ($\log(L_X) \lesssim 43.58$ erg s^{-1} at $z = 7.5$–15 for sources with observed $-20 \leq \log S(0.5\text{–}2) \leq -17$ erg cm^{-2} s^{-1}), source densities of the order of 1.5×10^{-4} and 8.4×10^{-5} Mpc^{-3} in the case of flat and declining evolution, respectively. The upper limit derived above suggests that the declining evolution of AGN is a good representation of the evolutionary track of these remote sources.

7 CONTRIBUTION OF UNDETECTED SOURCE POPULATIONS TO THE CXB

By interpreting the observed behaviour of the unresolved CXB fluctuations, we have developed a model that is able to explain the nature of the unresolved CXB. The fluctuations observed here are reproduced in the PS if the clustering recipes described in the text are combined with the unresolved CXB production rates shownin Table 2. Our results show that, in the 0.5–2 keV band, the effective fraction of the unresolved extragalactic background is of the order of 12 per cent of the total. In Table 2 we show the CXB flux that our model predicts to explain the fluctuations together with the fractions of total and unresolved CXB produced by every undetected source population. As one can see in Table 2, the bulk (∼56 per cent) of the unresolved CXB flux is made up of unresolved clusters, groups and the WHIM, which accounts by itself for ∼17 per cent of the unresolved flux.

For point sources, our model predicts that AGN and galaxies contribute, together, the remaining flux of the unresolved CXB, with galaxies and AGN producing ∼25 per cent and ∼20 per cent of the unresolved flux, respectively.

Table 1. (1) The χ^2/d.o.f. value for model with different components included and (2) the null-hypothesis probabilty obtained by adding an additional component with respect to the model with $n - 1$ d.o.f.

Model	χ^2/d.o.f. (1)	$P(F$-test) (2)
P_{SN}	43.4/13	
$P_{SN} + P_{Gal} + P_{AGN}$	17.5/12	1.2×10^{-3}
$P_{SN} + P_{IGM}$	18.3/12	1.6×10^{-3}
$P_{SN} + P_{Gal} + P_{AGN} + P_{IGM}$	7.8/11	2.7×10^{-3} *
$P_{SN} + P_{Gal} + P_{AGN} + P_{IGM} + P_{mq}$	8.3/10	*

*$P(F$-test$) = 7.9 \times 10^{-5}$ with respect to the SN-only model.

Moreover, our data cannot exclude the possibility that a sizeable fraction of the unresolved CXB could be produced by a population of still undetected high-z sources, likely black hole seeds.

8 DISCUSSION

In this paper we presented a measurement of the angular PS of the fluctuations of the unresolved CXB in 4-Ms observations of the CDFS in the angular range $\lesssim$10 arcmin. Poisson noise and spurious signals have been modelled and removed from the measured PS. We performed a spectral decomposition analysis and showed that after removing the low-frequency signal, which can be attributed to the shot noise of unresolved sources that randomly enter the beam, the amplitude of the fluctuations with extragalactic origin accounts for ∼12.3 per cent of the CXB and the significance of the detection of these cosmic fluctuations is $>10\sigma$. In the next section we briefly discuss the properties of the populations producing the unresolved CXB fluctuations.

8.1 The population of undetected AGN

For AGN, we folded the observed evolution scenarios with the population synthesis model of Gilli et al. (2007) and a simple recipe for bias, where AGN are tracing DMH with mass $\log(M) = 13.1\,M_\odot$.

This population of AGN has a space density that declines exponentially above $z = 2.7$. The CXB production rate necessary to produce the modelled PS yields a fraction of the unresolved 0.5–2 keV CXB flux of ∼19 per cent. We predicted a CXB flux produced by undetected AGN of $\sim 2.0 \times 10^{-13}$ erg cm^{-2} s^{-1} deg^{-2}.

We also tried to probe different evolution scenarios, but our data do not allow us to constrain the behaviour of the AGN XLF significantly at high z. In Fig. 9 we show the predicted $\log N - \log S$ that, according to our model, satisfies the observed fluctuations compared with recent observations.

8.2 The population of undetected X-ray galaxies

Galaxies are the most numerous population of objects contributing to the unresolved CXB (see Fig. 9); the power produced by such a population is lower that that of AGN since they are less biased even if they produce more CXB flux. In soft X-rays, galaxies have been observed up to $z \sim 1$ (see e.g. Lehmer et al. 2007) and therefore their high-z space density is unknown. We have developed a toy model for the galaxy XLF, where their evolution follows that of the star formation in the Universe. With this model we estimated

Table 2. (1) CXB production rate of every class of undetected sources, with the percentage of (2) overall and (3) unresolved CXB produced by every population. In the last line we show cumulative values; the ranges refer to Models I and II.

Component	S $\times 10^{-13}$ erg cm^{-2} s^{-1} deg^{-2} (1)	CXB[a] per cent (2)	Unres. CXB per cent (3)
AGN	1.97	2.4 ± 0.2	19.3 ± 1.3
Galaxies	2.51	3.1 ± 0.2	24.6 ± 1.7
IGM	5.70	7.0 ± 0.5	55.9 ± 3.9
[b]WHIM	1.70	2.1 ± 0.1	16.7 ± 1.2
Early BH	<0.35	<0.5	<3.4
Total	10.18	12.4 ± 0.9	100

[a] Computed using a total 0.5–2 keV CXB flux of $8.15 \pm 0.58 \times 10^{-12}$ erg cm^{-2} s^{-1} deg^{-2} (Lehmer et al. 2012).
[b] The WHIM flux is included in the IGM flux.

Downloaded from http://mnras.oxfordjournals.org/ at NASA Goddard Space Flight Ctr on July 14, 2014

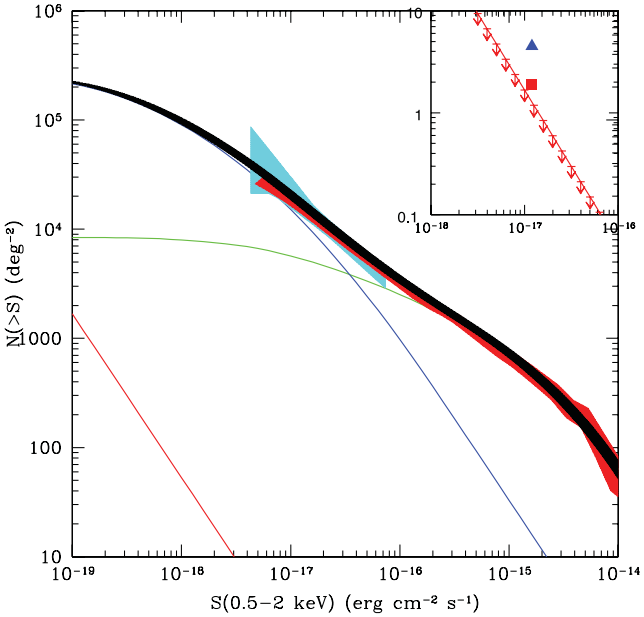

Figure 9. The 0.5–2 keV $\log N - \log S$ used to reproduce the observed unresolved CXB fluctuations. In AGN (green), galaxies (blue) and the sum of AGN and galaxies (black-shaded), the uncertainty is attributed to the count-rate to flux conversion. The long shaded area (red in the online article) is the $\log N - \log S$ measured by Lehmer et al. (2012) in the CDFS. The lower line (red in the online article) represents the upper limit of the $\log N - \log S$ of miniquasars. The smaller shaded area (cyan in the online article) represents the expected counts from the fluctuation analysis of Miyaji & Griffiths (2002). In the inset we show a zoomed-in view of the miniquasar upper limit $\log N - \log S$. The upward-pointing triangle (blue in the online article) is the expected number of X-ray sources at the flux limit of the 4-Ms CDFS produced at $z \lesssim 10$ from collapse of Pop. III stars accreting at the Eddington limit. The *red square* is the number of X-ray sources in the case of direct collapse (quasi-stars) accreting at $\lambda_{\rm Edd} = 0.3$.

that galaxies contribute ∼25 per cent of the unresolved CXB flux. In a recent paper, Dijkstra et al. (2012) used modelling similar to ours and found that, in principle, X-ray galaxies could produce all of the unresolved 1–2 keV CXB. However they did not consider the contribution of other undetected sources, which we have shown to produce a large fraction of the unresolved CXB. Overall, the predicted source counts of AGN and galaxies are in good agreement with the measurements of Xue et al. (2011) and Lehmer et al. (2012) in the same field.

8.3 CXB from IGM and WHIM

On scales larger than 100 arcsec, our analysis shows that the main contribution to unresolved CXB fluctuations is due to IGM emission produced by undetected groups, clusters and the WHIM. This has been estimated with cosmological hydrodynamical simulations that, together with structure formation, include feedback mechanisms that pollute the IGM with metals that are responsible for the X-ray emission (Roncarelli et al. 2012). Such a component produces ∼50 per cent of the unresolved CXB.

We determined that ∼1/3 of the IGM flux is produced by WHIM, where the so-called 'missing baryons' are expected to lie. However, the WHIM definition taken from simulations already applies a density cut ($\delta < 1000$) that is meant to mimic roughly the effect of excising detected sources. In reality, dense clumps may be present outside virialized objects so we must consider our determination as a lower limit of the total WHIM contribution (see the discussions in Roncarelli et al. 2006, 2012).

Our model thus predicts that the flux of WHIM in the CDFS is of the order of 1.7×10^{-13} erg cm^{-2} s^{-1} deg^{-2} (i.e. 2.3 per cent of the total CXB flux) and produces a signal peaking on a scale of a few arcmin. Such an estimate is about one order of magnitude lower than measured by Galeazzi et al. (2009) (i.e. 12 per cent of the overall diffuse emission in shallower 0.2–0.4 keV *XMM-Newton* observations), where they did not model the contamination from undetected sources. However such an estimate relies on the output of the simulation and is very sensitive to the metallicity of the WHIM. According to Roncarelli et al. (2012), different recipes for the metal enrichment of WHIM may lead to a variation of up to a factor of 3 in overall emissivity of the WHIM. Obtaining more information on such a component of the Universe would be possible if, for example, contamination of undetected clusters could be excised from X-ray maps by also masking optically detected groups with mass $\log(M) > 12$–$12.5\,{\rm M}_\odot$.

8.4 Very high-z sources

Finally, we speculated on the possible existence of a population of high-z miniquasars (or early black holes) born from the collapse of early massive objects. Although we did not detect their signature, we placed an upper limit on their contribution to the CXB ($<3 \times 10^{-13}/(1+z)$ erg cm^{-2} s^{-1} deg^{-2}, $z > 7.5$). We estimated that these sources would follow the declining evolutionary track of AGN with $\log(L_{\rm X}) \lesssim 43.58$ erg s^{-1}.

Our observations are not sensitive to the faint fluxes expected from these sources and thus we could only place upper limits. However, since such a population peaks at $z > 7.5$, their fluctuations should peak on scales of the order of several tens of arcmin, where the contribution from shot noise is also relatively weak in shallower surveys. On such a scale, the foreground source population PS significantly dims and therefore their detection would be possible. To conclude, we determined that at fluxes of the order 10^{-20} erg cm^{-2} s^{-1}, the number density of these sources is of the order of ∼60 000 deg^{-2}, which means that, under the assumption of Euclidean $\log N - \log S$, at the flux limit of the CDFS their number density is of the order of 1–2 deg^{-2}.

Using the theoretical predictions of Volonteri (2010), Treister et al. (2011) computed the expected number density of the first X-ray sources at $z \sim 7$–10 at the 4-Ms CDFS flux limit. In the case of Population III star remnants accreting at the Eddington limit they find 4.5 deg^{-2}, while in the case of direct collapse (quasi-stars: Begelman, Rossi & Armitage 2008) with an accretion regime at $\lambda_{\rm Edd} = 0.3$ their expected number density is 1.9 deg^{-2}. In Fig. 9 we show a comparison of these predictions with our upper limit which, at the zeroth order, favours the direct collapse scenario.

Our work suggests that future deeper observations on wider fields would allow us to improve the sensitivity of the PS measurement by reducing the shot noise and masking fainter clusters. Moreover, a deep survey with a flux limit comparable to or deeper to that of the 4-Ms CDFS covering 1–2 deg^2 would allow us a direct detection of the WHIM feature and, by measuring the large-scale shape of the PS, investigation of the very high-z X-ray Universe. A possible future X-ray mission like the proposed *Wide Field X-ray Telescope* (*WFXT*: Giacconi et al. 2009) will be able to study the PS of the unresolved CXB with high precision, given the large collecting area (low photon noise) and the large field of view (low cosmic variance).

Downloaded from http://mnras.oxfordjournals.org/ at NASA Goddard Space Flight Ctr on July 14, 2014

ACKNOWLEDGMENTS

NC acknowledges the INAF-Fellowship program for support. PA acknowledges support from Fondecyt 11100449. We acknowledge financial contribution from the agreement ASI-INAF 1/009/10/0. FN acknowledges support from NAS XMM Grant NNX08AX51G, XMM Grant NNX09AQ05G and ASI Grant ASI-ADAE. PR acknowledges a grant from the Greek General Secretariat of Research and Technology in the framework of the programme Support of Postdoctoral Researchers. NC thanks the anonymous referee for the suggested improvements.

REFERENCES

Adelberger K. L., Steidel C. C., Pettini M., Shapley A. E., Reddy N. A., Erb D. K., 2005, ApJ, 619, 697
Allevato V. et al., 2011, ApJ, 736, 99
Arevalo P., Churazov E., Zhuravleva I., Hernandez-Monteagudo C., Revnivtsev M., 2012, preprint (arXiv:1207.5825)
Barcons X., Fabian A. C., Carrera F. J., 1998, MNRAS, 293, 60
Bauer F. E., Alexander D. M., Brandt W. N., Schneider D. P., Treister E., Hornschemeier A. E., Garmire G. P., 2004, AJ, 128, 2048
Begelman M. C., Rossi E. M., Armitage P. J., 2008, MNRAS, 387, 1649
Bonoli S., Marulli F., Springel V., White S. D. M., Branchini E., Moscardini L., 2009, MNRAS, 396, 423
Bouwens R. J. et al., 2011, ApJ, 737, 90
Brandt W. N. et al., 2001, AJ, 122, 2810
Brunner H., Capelluti N., Hasinger G., Barcons X., Fabian A. C., Mainieri V., Szokoly G., 2008, A&A, 479, 283
Brusa M. et al., 2009, ApJ, 693, 8
Cappelluti N. et al., 2009, A&A, 497, 635
Cappelluti N., Allevato V., Finoguenov A., 2012, Adv. Astron., 2012, 853701
Cen R., Ostriker J. P., 1999, ApJ, 514, 1
Churazov E. et al., 2012, MNRAS, 421, 1123
Civano F. et al., 2011, ApJ, 741, 91
da Ângela J. et al., 2008, MNRAS, 383, 565
Diego J. M., Sliwa W., Silk J., Barcons X., 2003, MNRAS, 344, 951
Dijkstra M., Gilfanov M., Loeb A., Sunyaev R., 2012, MNRAS, 421, 213
Eckmiller H. J., Hudson D. S., Reiprich T. H., 2011, A&A, 535, A105
Fabian A. C., Barcons X., 1992, ARA&A, 30, 429
Fang T., Buote D. A., Humphrey P. J., Canizares C. R., Zappacosta L., Maiolino R., Tagliaferri G., Gastaldello F., 2010, ApJ, 714, 1715
Finoguenov A. et al., 2007, ApJS, 172, 182
Fiore F. et al., 2012, A&A, 537, 16
Fukugita M., Hogan C. J., Peebles P. J. E., 1998, ApJ, 503, 518
Galeazzi M., Gupta A., Ursino E., 2009, ApJ, 695, 1127
Giacconi R. et al., 2001, ApJ, 551, 624
Giacconi R. et al., 2009, astro2010: The Astronomy and Astrophysics Decadal Survey, Science White Papers, no. 90
Gilli R., Risaliti G., Salvati M., 1999, A&A, 347, 424
Gilli R., Comastri A., Hasinger G., 2007, A&A, 463, 79
Hasinger G., Miyaji T., Schmidt M., 2005, A&A, 441, 417
Helgason K., Ricotti M., Kashlinsky A., 2012, ApJ, 752, 113
Hickox R. C., Markevitch M., 2006, ApJ, 645, 95
Hickox R. C., Markevitch M., 2007, ApJ, 661, L117
Hopkins P. F., Lidz A., Hernquist L., Coil A.L., Myers A. D., Cox T. J., Spergel D. N., 2007, ApJ, 662, 110
Kaastra J. S., Werner N., den Herder J. W. A., Paerels F. B. S., de Plaa J., Rasmussen A. P., de Vries C. P., 2006, ApJ, 652, 189
Kaiser N., 1984, ApJ, 284, L9
Kashlinsky A., 2005, Phys. Rep., 409, 361
Kashlinsky A., Arendt R. G., Mather J., Moseley S. H., 2005, Nat, 438, 45
Kashlinsky A., Arendt R. G., Mather J., Moseley S. H., 2007, ApJ, 654, L5
Kashlinsky A., Arendt R. G., Ashby M. L. N., Fazio G. G., Mather J., Moseley S. H., 2012, ApJ, 753, 63
Lehmer B. D. et al., 2007, ApJ, 657, 681
Lehmer B. D. et al., 2012, ApJ, 752, 46
Lemze D., Sadeh S., Rephaeli Y., 2009, MNRAS, 397, 1876
Lewis A., Bridle S., 2002, Phys. Rev. D, 66, 103511
Luo B. et al., 2008, ApJS, 179, 19
Martin-Mirones J. M., de Zotti G., Franceschini A., Boldt E. A., Marshall F. E., Danese L., Persic M., 1991, ApJ, 379, 507
Matsumoto T. et al., 2011, ApJ, 742, 124
Miyaji T., Griffiths R. E., 2002, ApJ, 564, L5
Moretti A., Campana S., Lazzati D., Tagliaferri G., 2003, ApJ, 588, 696
Nicastro F. et al., 2005, Nat, 433, 495
Ouchi M. et al., 2004, ApJ, 611, 685
Peebles P. J. E., 1980, The Large Scale Structure of the Universe. Princeton Univ. Press, Princeton
Ptak A., Griffiths R., White N., Ghosh P., 2001, ApJ, 559, L91
Ranalli P., Comastri A., Setti G., 2005, A&A, 440, 23
Robertson B. E., 2010, ApJ, 716, L229
Roncarelli M., Moscardini L., Tozzi P., Borgani S., Cheng L. M., Diaferio A., Dolag K., Murante G., 2006, MNRAS, 368, 74
Roncarelli M., Cappelluti N., Borgani S., Branchini E., Moscardini L., 2012, MNRAS, 424, 1012
Setti G., Woltjer L., 1989, A&A, 224, L21
Sheth R. K., Mo H. J., Tormen G., 2001, MNRAS, 323, 1
Shull J. M., Smith B. D., Danforth C. W., 2012, ApJ, preprint (arXiv:1112.2706)
Smith R. E. et al., 2003, MNRAS, 341, 1311
Sołtan A. M., 2006, A&A, 460, 59
Soltan A., Hasinger G., 1994, A&A, 288, 77
Sołtan A. M., Freyberg M. J., Hasinger G., 2002, A&A, 395, 475
Tornatore L., Borgani S., Viel M., Springel V., 2010, MNRAS, 402, 1911
Treister E., Urry C. M., 2006, ApJ, 652, L79
Treister E., Schawinski K., Volonteri M., Natarajan P., Gawiser E., 2011, Nat, 474, 356
Ursino E., Galeazzi M., 2006, ApJ, 652, 1085
van den Bosch F. C., 2002, MNRAS, 331, 98
Volonteri M., 2010, A&AR, 18, 279
Wu X., Anderson S. F., 1992, AJ, 103, 1
Xue Y. Q. et al., 2011, ApJS, 195, 10
Śliwa W., Soltan A. M., Freyberg M. J., 2001, A&A, 380, 397

This paper has been typeset from a TEX/LATEX file prepared by the author.

Downloaded from http://mnras.oxfordjournals.org/ at NASA Goddard Space Flight Ctr on July 14, 2014